12-1-2008

Brain-Tumor Interaction Biophysical Models for Medical Image Registration

Cosmina Hogea
University of Pennsylvania

Christos Davatzikos
University of Pennsylvania, christos@rad.upenn.edu

George Biros
University of Pennsylvania, biros@seas.upenn.edu

Publisher URL: http://dx.doi.org/10.1137/07069208X

SIAM J. SCI. COMPUT.
Vol. 30, No. 6, pp. 3050–3072

BRAIN–TUMOR INTERACTION BIOPHYSICAL MODELS FOR MEDICAL IMAGE REGISTRATION*

COSMINA HOGEA†, CHRISTOS DAVATZIKOS†, AND GEORGE BIROS‡

Abstract. State-of-the art algorithms for deformable image registration are based on the minimization of an image similarity functional that is regularized by adding a penalty term on the deformation map. The penalty function typically represents a smoothness regularization. In this article, we use a constrained optimization formulation in which the image similarity functional is coupled to a biophysical model. This formulation is pertinent when the data have been generated by imaging tissue that undergoes deformations due to an actual biophysical phenomenon. Such is the case of coregistering tumor-bearing brain images from the same individual. We present an approximate model that couples tumor growth with the mechanical deformations of the surrounding brain tissue. We consider primary brain tumors—in particular, gliomas. Glioma growth is modeled by a reaction-advection-diffusion PDE, with a two-way coupling with the underlying tissue elastic deformation. Tumor bulk, infiltration, and subsequent mass effects are not regarded separately but are captured by the model itself in the course of its evolution. Our formulation allows for updating the tumor diffusion coefficient following structural displacements caused by tumor growth/infiltration. Our forward problem implementation builds on the `PETSc` library of Argonne National Laboratory. Our reformulation results in a very small parameter space, and we use the derivative-free optimization library `APPSPACK` of Sandia National Laboratories. We test the forward model and the optimization framework by using landmark-based similarity functions and by applying it to brain tumor data from clinical and animal studies. State-of-the-art registration algorithms fail in such problems due to excessive deformations. We compare our results with previous work in our group, and we observed up to 50% improvement in landmark deformation prediction. We present preliminary validation results in which we were able to reconstruct deformation fields using four degrees of freedom. Our study demonstrates the validity of our formulation and points to the need for richer datasets and fast optimization algorithms.

Key words. medical image registration, tumor growth, deformable registration, soft-tissue simulations

AMS subject classifications. 65N50, 65Y05, 68W10, 68W15

DOI. 10.1137/07069208X

1. Introduction.

Medical image registration (see Figure 2) involves the construction of point-correspondences between a set of images: given a target image τ, a series of images $\sigma(t)$ parametrized by time t, and an image similarity functional $\mathcal{J}(\tau, \sigma)$, we would like to construct a deformation map $\boldsymbol{\psi}^*(t)$ such that

$$\boldsymbol{\psi}^* = \arg\min_{\boldsymbol{\psi}} \mathcal{J}(\sigma \circ \boldsymbol{\psi}, \tau) + \mathcal{R}(\boldsymbol{\psi}). \tag{1.1}$$

The penalty term $\mathcal{R}$ is introduced to generate anatomy-preserving deformations. Typically, $\mathcal{R}$ represents an energy term that ensures that ψ is a diffeomorphism [6, 11, 18, 43]. We do not attempt to review the extensive literature on formulations

*Received by the editors May 16, 2007; accepted for publication (in revised form) June 16, 2008; published electronically October 13, 2008. A preliminary version of this article was presented at the 2007 SIAM Conference on Computational Science and Engineering [31].
http://www.siam.org/journals/sisc/30-6/69208.html
†Section of Biomedical Image Analysis, Department of Radiology, University of Pennsylvania, Philadelphia, PA 19104 (hogeac@uphs.upenn.edu, christos@rad.upenn.edu).
‡Departments of Mechanical Engineering and Applied Mechanics, Bioengineering, and Computer and Information Science, University of Pennsylvania, Philadelphia, PA 19104 (biros@seas.upenn.edu).

and solution methodologies for (1.1). An excellent introduction on this topic can be found in [44].

In this article, we expand our work in [29] and discuss a formulation for the case in which $\boldsymbol{\psi}$ is related to a biophysical phenomenon, the so-called *mass effect*: the mechanical deformation of healthy brain tissue due to cancerous tumor growth. We reformulate (1.1) by replacing $\mathcal{R}$ with biophysical constraints on $\boldsymbol{\psi}$:

$$(\boldsymbol{\psi}^*, \boldsymbol{\phi}^*, \boldsymbol{g}^*) = \arg\min_{\boldsymbol{\psi},\boldsymbol{\phi},\boldsymbol{g}} \mathcal{J}(\sigma \circ \boldsymbol{\psi}, \tau) \quad \text{subject to} \quad F(\boldsymbol{\phi}, \boldsymbol{\psi}, \boldsymbol{g}) = 0. \tag{1.2}$$

In addition to the map $\boldsymbol{\psi}$, we have introduced the biophysical variables $\boldsymbol{\phi}$ and unknown parameters $\boldsymbol{g}$. The nonlinear map F represents the biophysical model, a reaction-advection-diffusion tumor growth model coupled to elasticity. In the brain–tumor interaction case, $\boldsymbol{\phi}$ comprises two components: the tumor concentration and the displacement. $\boldsymbol{g}$ consists of the diffusion and reaction coefficients, parametrizations of the initial tumor concentration, and the force coupling between the tumor and the tissue. We use a landmark-based similarity functional $\mathcal{J}$, which is mathematically equivalent to having discrete observations on $\boldsymbol{\psi}$.

The main advantage of the constrained optimization formulation is that it incorporates problem-specific prior information—instead of a generic $\mathcal{R}$—related to the underlying biophysical phenomenon. By using more informed priors, we can produce complex deformation maps using small parameter spaces (in the case we discuss in this paper, we use only four parameters).[1]

The main drawback of our approach is that strong priors may lead to strong bias—that is, if they are wrong. Indeed, there is significant uncertainty associated with the exact form of F and its interindividual variability. Additional drawbacks of our approach over standard regularization techniques include computational challenges in simulating F and the fact that our formulation is not applicable to image registration across different individuals since there is no underlying physical deformation that follows a biophysical law. In the following, we describe the clinical problem, the biophysical model, the related work, our contributions, and the limitations in our approach.

Motivation. More than 50% of primary brain tumors are gliomas, which are seldom treatable with resection, and which ultimately progress to high-grade tumors, leading to death in only 6–12 months [1]. A better understanding of the characteristics of the progression of brain cancer, based on phenotypic cancer profiles derived from imaging, histopathology, and other sources, can help to determine predictive factors for cancer invasion. A significant tool for understanding such cancer profiles is the construction of statistical atlases ("an average brain").

Statistical atlases of brain function and structure have been widely used as a means of integrating diverse information about anatomical and functional variability into a canonical coordinate space (often called a stereotactic space) for better understanding and diagnosing of brain diseases [5, 13]. In the case of brain tumor patients, such atlases have the potential to assist surgical and treatment planning. In order to construct and use brain tumor atlases, tumor-bearing patient images must be coregistered to normal brain images or a statistical atlas; i.e., a transformation

[1]The constrained formulation can be viewed as a nonlinear transformation on $\boldsymbol{\psi}$. Instead of solving for $\boldsymbol{\psi}$, we solve for $\boldsymbol{g}$. If we knew the Lagrange multipliers associated with the Euler–Lagrange optimality conditions for (1), then (1.2) would be just a special case of (1.1). But the Lagrange multipliers are not known. Thus, (1.2) is different from (1.1) in both analytical and computational aspects.

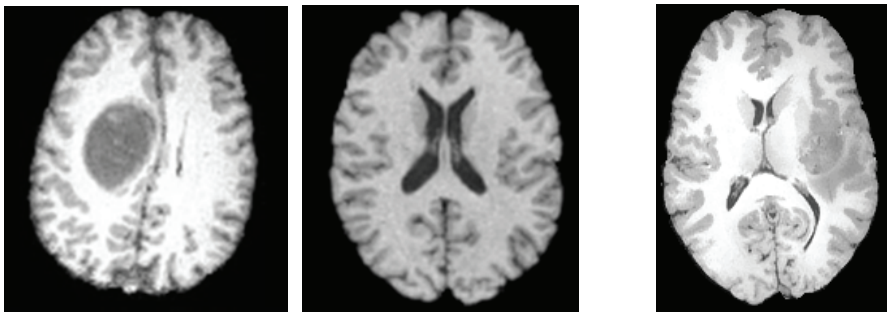

FIG. 1. IMAGE REGISTRATION. *Given two images* (a) *and* (b) *we would like to find anatomical correspondences between them. Image* (a) *is an axial slice from an MR (magnetic resonance) image of a patient with tumor. Image* (b) *can be a statistical atlas, or an MR image of the patient before the tumor occurrence. Mapping image* (a) *to image* (b) *is unusually hard because of the topological differences and the large deformations due to the presence of the tumor. If one uses standard deformable registration methods, there will be significant errors, particularly in areas near the tumor. In image* (c)*, we show a second example, an axial slice from an MR image of a patient diagnosed with Glioblastoma multiforme grade* IV*. This image illustrates the highly infiltrative nature of such tumors which leads to a poorly defined brain–tumor interface and a strong mass effect.*

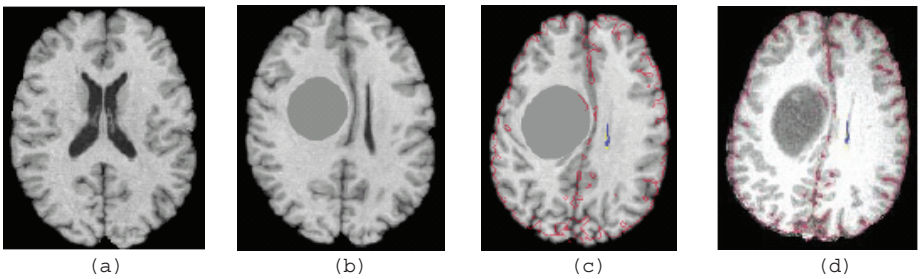

FIG. 2. BIOPHYSICALLY CONSTRAINED REGISTRATION OF TUMOR-BEARING BRAIN IMAGES. *Schematic illustration of a multistep simulation designed to improve the deformable registration process from tumor-bearing patient images to normal brain templates. Instead of attempting to directly register two highly dissimilar images (images* (a) *and* (d))*, we construct a tumor-bearing brain atlas (image* (b)*) and then register the tumor-bearing template to the actual patient image to obtain image* (c)*. In this way, the original problem of constructing a map between two highly dissimilar images is the composition of two deformations:* (a) *to* (b) *and* (b) *to* (d)*. In this article, we consider the simpler problem of constructing a deformation map between images of a single individual taken at different points in time.*

must be constructed between the image with the brain tumor and a given normal brain template. Existing brain image registration methods that attempt to directly register two such objects typically come up short in the presence of large tumors and subsequent mass effect, such as the case depicted in Figure 1.

Here, we present a scheme that couples a mass-effect model with image registration, as depicted in Figure 2. To aid the registration process, particularly in areas close to the tumor, it is helpful to first construct a brain atlas that has tumor and mass effects similar to the images of the patients in our study. Subsequent deformable registration is than more likely to better match the atlas to the patient's images, since it has to solve a problem involving two brains that are relatively similar, compared to matching a normal atlas with a highly deformed brain [12, 15, 37]. This involves a

simulation pipeline in which tumor simulation is the first step, followed by registration, as illustrated schematically in Figure 2.[2]

1.1. Related work. Biophysically induced deformations have motivated the form of the smoothness regularization term in (1.1). Indeed, researchers often inject biomechanical information, such as elastic constants and anisotropy directions, into $\mathcal{R}$ [16,33,40,48,55]. This, however, is not equivalent to having the correct biophysics, as multiphysics couplings, boundary conditions, and distributed forces are not included in $\mathcal{R}$. To our knowledge, the only work similar to ours is [38], the authors of which consider a mechanical model (without tumors) for parenchymal shift. The inversion parameters are distributed forces.

Tumor growth models. Most of the work in tumor growth models has involved in vitro experimental setups (to allow for validation). The two main approaches are discrete [34] and continuous [3]. Cellular automata (CA), or lattice-based models, belong to the discrete setting. Probabilistic phenomenological rules are used for the spatiotemporal evolution of each cell (e.g., mitosis, apoptosis, chemotaxis, random motion). The continuous approach is typically based on macroscopic conservation laws expressed via PDEs [14]. Another approach involves reaction-diffusion models [50,52]. More complex models have multiple species, take into account cellular heterogeneity, and incorporate mechanical effects in tissues [4, 10, 52].

Brain–tumor interaction. In [26, 28, 46], a purely mechanical model was used to simulate the tumor–brain interface evolution and the mass effect. The brain tissue was modeled as a nonlinearly elastic material. A cavity representing the tumor was introduced and a pressure-like Neumann condition was used to model tumor-induced interface forces. This method has two main limitations: (1) it has difficulty capturing more irregularly shaped tumors (the simulated tumors are generally quasi-spherical); and (2) it provides no information about the actual tumor evolution and its infiltration into healthy tissue. In [12], the authors have used an approach similar to ours: they modeled the mass effect caused by the tumor bulk and added a separate reaction-diffusion model (similarly to [24, 50, 52]) to account for the tumor infiltrative part only. In their method the tumor reaction-diffusion equation is decoupled from the elasticity equations and the diffusion coefficient. No optimization framework was used in that work.

1.2. Contributions and limitations. Given a time sequence of tumor-bearing images from *the same* individual we seek to coregister them. Toward that goal, we propose a model that couples glioma growth with the deformation of the brain tissue. Building upon the work of [50] and our own work [29], glioma growth is modeled via a nonlinear reaction-advection-diffusion equation coupled to an elastic deformation model (ten variables per grid point). The overall modeling framework results in a strongly coupled nonlinear system of PDEs. The main differences compared to prior work are that (1) there is no sharp-interface separation between a tumor bulk and an infiltrative part; (2) the tissue deformation causes spatial changes in the distribution of the diffusion coefficient and advects the tumor concentration; and (3) the solver is coupled with the image-registration optimization problem. Besides synthetic datasets, we use data from clinical and animal studies for the preliminary validation of our model.

[2]Due to its complexity and high computational cost, our approach is more appropriate for atlas construction and pre- and postoperative analysis rather than for open MR-type intraoperative registration (see [55]).

In a nutshell, the main contributions of this paper are as follows:

- A forward problem formulation and numerical scheme for image-driven multiphysics deformations;
- a numerical study of the constrained-optimization formulation for the case of landmark registration;
- application of the scheme to images of tumor-bearing brains, and its preliminary validation.

The forward problem solver is based on an operator-split semi-implicit scheme, which is first-order accurate in space and time. In general, we expect large deformations. To avoid bottlenecks associated with unstructured meshes, we use a structured grid approach and employ a penalty approach to impose boundary conditions on internal boundaries.

We solve (1.2) for a parametrization of the tumor initial condition, the diffusion and reaction coefficients, and a parametrization of the distributed pressure exerted on the parenchyma due to the gradient of the tumor concentration. To our knowledge, the proposed model is not only one of the first attempts to directly couple mechanics with diffusion-reaction transport models for tumor growth but also the first one that states an image-driven constrained optimization problem. We have opted to postpone the integration of our model with a gradient-descent-based optimization. Instead, we use a derivative-free algorithm. Our main goal is a preliminary validation of our methodology on real data. The overall results are encouraging.

Limitations. Our goal is to develop tools for registration of tumor-bearing brain images to templates. Here, we consider the simpler problem of intraindividual registration, which requires images of the same patient acquired at different points in time (also called *longitudinal images*). The requirement of longitudinal datasets is a limitation because in the majority of clinical cases, early stage scans are not available (typically, the patients are immediately treated with surgery, chemotherapy, and/or radiation).

We employ a landmark-based registration approach. We identify the landmarks by manually preprocessing the images. A more general approach would employ intensity-based registration methods; this is part of ongoing work. One difficulty is that the biophysical model requires segmentation of the images in order to assign material properties. Automatic segmentation, especially for tumor-bearing images, is an open problem. Overall, our current implementation requires landmark extraction and segmentation. We have quantified rater variability for the landmark extraction. Quantification of rater variability for the segmentation is part of our ongoing investigation.

Currently, we parametrize the motion using only four parameters. In particular, we assume that the location of the center of the tumor is known. In general, this is a strong assumption. The center is ill-defined and requires further manual processing. In [32], we discuss a solution algorithm (applied in a synthetic 1D problem) in which we do not parametrize the initial concentration of the tumor but instead solve for it at every point in space. In this paper, our first attempt to couple optimization with real datasets, we decided to use the simplest possible formulation, and we assume that the center of the tumor in the initial frame is given.

Let us reiterate that the purpose of the proposed method is image registration. The chosen biomechanical model cannot be used to predict either tumor growth or mechanical deformations without image information because it is too simplified. More complex models typically include several undetermined parameters that render

calibration, validation, and sensitivity analysis difficult. As we acquire additional datasets from clinical and animal studies, more complex models can be introduced and validated.

1.3. Organization of the paper. In section 2 we introduce the biophysical model (forward problem) and the associated registration problem. The problem solved in this work is stated in (2.6). We discuss discretization and numerics in section 3. In section 4 we apply our method to synthetic and clinical data. We perform a parametric study to experimentally assess the nonconvexity of the optimization problem. We also employ cross validation to assess the predictive capabilities and shortcomings of our approach.

2. Biophsysical model. In this section, we discuss the tumor growth model, the mechanical deformation model for the brain tissue, and their coupling. In all cases, the domain of interest is the intracranial space. All equations are expressed in an Eulerian (or spatial) frame of reference [23].

Tumor growth model. To our knowledge, there exist no tumor growth models that are quantitatively predictive. This fact, along with computational efficiency considerations and limited in vivo data (typically, two to three preoperative images per patient), has led us to opt for models that are as simple as possible.

The main effects that we are interested in capturing are spatiotemporal spread of gliomas and the subsequent mass effects. This model is based on the following assumptions:

- The tumor is regarded as a single species described by its concentration (number of cells in a control volume); we do not account for tumor cell heterogeneity (e.g., living tumor cells, dead cells, endothelial cells).
- Tumor cells undergo mitosis, random motion (diffusion), and transport motion (advection); tumor cell death occurs once the concentration reaches a saturation value.

Under these assumptions, we adopt a scalar reaction-advection-diffusion tumor growth model [12, 50, 51] as follows:

$$\frac{\partial c}{\partial t} = \nabla \cdot (D \nabla c) - \nabla \cdot (c\mathbf{v}) + \rho \frac{c(c_s - c)}{c_s} \quad \text{in} \quad U.$$

Here $U = \omega \times (0, T)$, with ω being the interior of the skull; c is the tumor concentration, $\mathbf{v}$ is the velocity, ρ and D are reaction and diffusion coefficients, and c_s is the tumor saturation level (bulk tumor) and is normalized to $c_s = 1$. We assume an isotropic and inhomogeneous (piecewise-constant) diffusion coefficient derived from the segmented MR image (see Figure 3).[3] Typically, we segment three regions: white matter, gray matter, and cerebrospinal fluid which includes the ventricles.

Following [50], the tumor diffusivity in the white matter was set five times higher than in the gray matter. The diffusivity in the ventricles and cerebrospinal fluid is set to zero. In the bulk tumor we have $c \approx c_s$; in regions where $c \ll c_s$ (infiltration), a proliferation term ρc corresponding to exponential growth at rate ρ is retrieved [50]. Proliferation is assumed to slow down when $c \approx c_s$, and it eventually becomes a death term if c becomes larger than c_s. The tumor cell drift velocity $\mathbf{v}$ depends

[3] Experimental evidence [20] suggests that tumor diffusion may be transversely isotropic in the white matter and isotropic in the gray matter. Here, for simplicity, we shall consider the case of isotropic diffusion in both the white and the gray matter, with diffusion coefficients D_w and D_g, respectively.

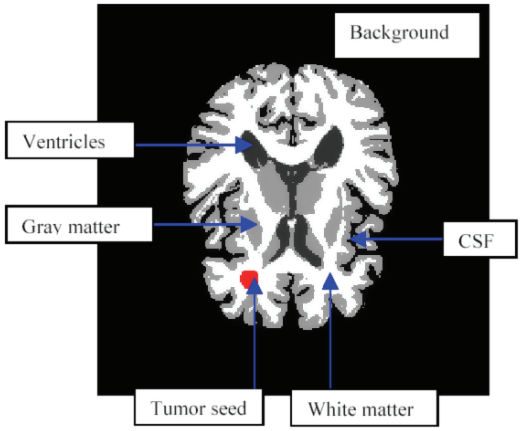

FIG. 3. SEGMENTATION. *Segmented MR image: Axial slice, illustrating different structures (white matter, gray matter, ventricles, cerebrospinal fluid) in the brain, with an initial tumor seed overlaid. In our simulations we use a segmented MR image to define material properties (here, elastic parameters and tumor cell diffusivity). Each segmentation label is converted to the corresponding material property via a look-up table.*

on chemotaxis and other unmodeled tumor-specific mechanisms. Our model only accounts for the tumor cells being displaced as a consequence of the underlying tissue mechanical deformation. The tumor model is augmented by initial and boundary conditions. The initial condition for the tumor depends on the problem at hand. In [30], we solve for a distributed parametrization of the initial conditions by using a PDE-constrained optimization algorithm (in one dimension). Here we assume a Gaussian initial tumor profile

$$c(\mathbf{x},0) = c_0 e^{-\frac{|\mathbf{x}-\mathbf{x}_0|^2}{2\sigma^2}}, \qquad c_0 > 0.$$

The center and support of the Gaussian are determined manually by inspecting the input image; c_0 is one of the variables in the parameter estimation problem. We use a zero-flux boundary condition at the skull.

Deformation model. Roughly speaking, the brain behaves as a nonlinear viscoelastic, anisotropic, and inhomogeneous material. An excellent review of the related literature on constitutive models for the brain parenchyma can be found in [45]. More detailed discussions can be found in [19, 41, 42]. We have adopted a simpler model for various reasons. First, there are no known techniques for determining noninvasively the mechanical properties of the brain tissue. So a generic model for all individuals must be assumed. Second, there is no consensus on a constitutive model for the brain [45]. Third, the presence of a tumor significantly alters the material properties of the tissue due to infiltration and proliferation, introducing additional uncertainties.

So, given the multiple sources of uncertainty, we make the following assumptions:

- We approximate the mechanics of the brain tissue (including tumor) using a linear elastic inhomogeneous material. Various values for the elastic material properties E and ν of the brain have been proposed [25].
- Although these elastic constants cannot be used for the tumor, we assume that the tumor does not alter the mechanical properties of the background tissue. This assumption is known to be invalid in practice.

- Given the tumor growth time scales (months), we use a quasi-static approximation and neglect inertial terms. Simple modal analysis can show that this is a quite reasonable assumption.
- We assume that the parenchyma behaves as a Maxwell viscoelastic solid. We assume that the strain relaxation time scale is much smaller than the tumor growth scale; therefore, the residual stresses and strains are zero. Brain tissue is viscoelastic, but there are no experiments that support our assumption.

Under these assumptions, in an Eulerian frame of reference the motion is described by

$$\rho\dot{\mathbf{v}} = \nabla\cdot\mathbf{T} + \mathbf{b} \quad \text{in } U \text{ (momentum)}, \quad \mathbf{T} = \widehat{\mathbf{T}}(\mathbf{F}, \dot{\mathbf{F}}) \quad \text{in } U \text{ (constitutive)},$$
$$\dot{\mathbf{F}} = \nabla\mathbf{v}\mathbf{F}, \mathbf{v} = \dot{\mathbf{u}} \quad \text{in } U \text{ (kinematics)}, \quad \dot{\mathbf{m}} = 0 \quad \text{in } U \text{ (material properties)}.$$

Here $\mathbf{v}$ is the velocity field, $\mathbf{u}$ is the displacement field, $\mathbf{b}$ is a distributed force, $\mathbf{T}$ is the Cauchy stress tensor, and $\widehat{\mathbf{T}}$ denotes the constitutive law depending on the deformation tensor $\mathbf{F} = \mathbf{I} + \nabla\mathbf{u}$ and its material time derivative $\dot{\mathbf{F}}$.[4] Here $\mathbf{m}$ denotes material properties that are advected with the underlying material motion. Here we employ the linear elasticity theory and approximate the brain tissue as a linear elastic inhomogeneous material $\mathbf{T} = \lambda\nabla\cdot\mathbf{u} + \mu(\nabla\mathbf{u} + \nabla\mathbf{u}^T)$, where λ and μ are the spatially varying Lamé's coefficients.[5]

The equations of motion need to be augmented with appropriate initial and boundary conditions. The initial conditions are easy; the initial velocity and displacement fields are zero.[6] We have imposed zero Dirichlet conditions on the boundary of ω (skull); this is not the most accurate choice; a better one would have been a mixed condition with zero displacements in the normal direction, and zero stresses in the tangential direction, to allow for sliding over the brain surface [46]. Given the multiple sources of error in the model, however, the boundary conditions play a secondary role. In [29], we conducted parametric studies that show that the errors in the boundary conditions do not play a significant role in the quality of registration.

While for white and gray matter there is a range of values frequently employed in the biomechanics community [25], there is no established approach for the tumor (studies have shown that the tumor is stiffer). The ventricles are filled with cerebrospinal fluid. A physically sound approach would be to use a fluid-structure interaction approach, with a Stokesian fluid for the ventricles. Given the overall uncertainty in the model, and to maintain reduced computational complexity, we approximate the ventricles by a very soft and compressible elastic material.

In all of our experiments, we use $E_{white} = 2100\,\text{Pa}$ and $E_{ventricles} = 500\,\text{Pa}$ for the Young's modulus for the white matter and ventricles, respectively, and we use $\nu_{white} = 0.45$ and $\nu_{ventricles} = 0.1$ for the Poisson's ratio for the white matter and ventricles, respectively. The values of the Young's modulus and the Poisson's ratio in the gray matter are exactly the same as those values in the white matter.

Brain–tumor coupling. We assume that the tumor is exerting a distributed (volumetric) body force $\mathbf{b}$ to the brain parenchyma; this force is assumed to be a pressure proportional to the gradient of the tumor concentration. This pressure causes the

[4] The material time derivative operator of a field (scalar, vector, tensor) $\mathbf{f}$ is defined as $\dot{\mathbf{f}} = \frac{\partial\mathbf{f}}{\partial t} + (\nabla\mathbf{f})\mathbf{v}$.

[5] Lamé's constants are related to Young's modulus E (stiffness) and Poisson's ratio ν (compressibility) by $\lambda = \frac{E\nu}{(1-2\nu)(1+\nu)}$ and $\mu = \frac{E}{2(1+\nu)}$.

[6] One has first to write the equations of motion and then invoke the quasi-static approximation.

tissue to deform. Following [12] and [56], we assume that $\mathbf{b} = -f(c)\nabla c$, where

$$f(c) = p_1 e^{-\frac{p_2}{(c/c_s)^2}} e^{-\frac{p_2}{(2-c/c_s)^2}},$$

and p_1, p_2 are positive constants. This function is monotonically increasing for $0 < c \leq c_s$ and has a maximum at $c = c_s$; p_1 controls the magnitude, whereas p_2 controls the nonlinear term in f. We discuss the effect of p_1 and p_2 in later sections.

Overall formulation of the forward problem. Let us summarize as follows the coupled system of PDEs governing our deformable model for simulating glioma growth and the subsequent mass effects:

$$\frac{\partial c}{\partial t} - \nabla \cdot (D\nabla c) + \nabla \cdot (c\mathbf{v}) - \rho c \left(\frac{c_s - c}{c_s}\right) = 0, \tag{2.1}$$

$$\nabla \cdot ((\lambda \nabla \cdot \mathbf{u}) + \mu(\nabla \mathbf{u} + \nabla \mathbf{u}^T)) - f\nabla c = 0, \tag{2.2}$$

$$\mathbf{v} = \frac{\partial \mathbf{u}}{\partial t}, \tag{2.3}$$

$$\frac{\partial \mathbf{m}}{\partial t} + (\nabla \mathbf{m})\mathbf{v} = 0. \tag{2.4}$$

The expression (2.3) of the velocity field $\mathbf{v}$ holds under the assumption of small strains; $\mathbf{m} = (\lambda, \mu, D)$. Since we are using an Eulerian frame of reference, inhomogeneous material properties like λ, μ, and the tumor cell diffusivity D need to be updated (advected) to follow the motion of the underlying tissue. For brevity, we write (2.1)–(2.4) as

$$\frac{\partial \boldsymbol{\phi}}{\partial t} + \mathbf{F}(\boldsymbol{\phi}, \boldsymbol{g}) = 0, \tag{2.5}$$

where $\boldsymbol{\phi} = (c, \mathbf{u}, \mathbf{v}, \mathbf{m})$ denotes the state variables. Also, we have introduced the vector of parameters $\boldsymbol{g}$ that will be determined by solving the image-registration problem.

2.1. Image registration. We propose a biomechanically constrained optimization approach, which we solve to estimate the deformation parameters. As we discussed in the introduction, instead of an intensity-based functional [44], in this initial implementation we follow a landmark-based registration method.

We consider the case of longitudinal data (i.e., serial scans over a period of time) for a brain tumor subject. We use landmark registration [8]. Given model-generated landmarks and manually tracked landmarks, we seek to find a deformation that minimizes the mismatch between the predicted and the actual deformation (see Figure 4). Let $\{\mathbf{x}_l^k\}_{l=1,\ldots,L;\ k=1,\ldots,N}$ be the manually placed landmarks at times $0 < \{t_k\}_{k=1}^N \leq T$. Then, (1.2) becomes

$$\begin{aligned} \min_{\boldsymbol{\phi},\psi,\boldsymbol{g}} J &:= \sum_{k=1}^{N} \sum_{l=1}^{L} \left|\boldsymbol{\psi}(\mathbf{x}_l^k, t) - \mathbf{x}_l^k\right| \\ &\text{subject to} \\ \frac{\partial \boldsymbol{\phi}}{\partial t} &+ \mathbf{F}(\boldsymbol{\phi}, \boldsymbol{g}) = 0; \\ \frac{\partial \boldsymbol{\psi}}{\partial t} + (\nabla \boldsymbol{\psi})\mathbf{v} = 0, &\quad \boldsymbol{\psi}(\mathbf{x}, t = 0) = \mathbf{x}; \\ \boldsymbol{g}_L &\leq \boldsymbol{g} \leq \boldsymbol{g}_U. \end{aligned} \tag{2.6}$$

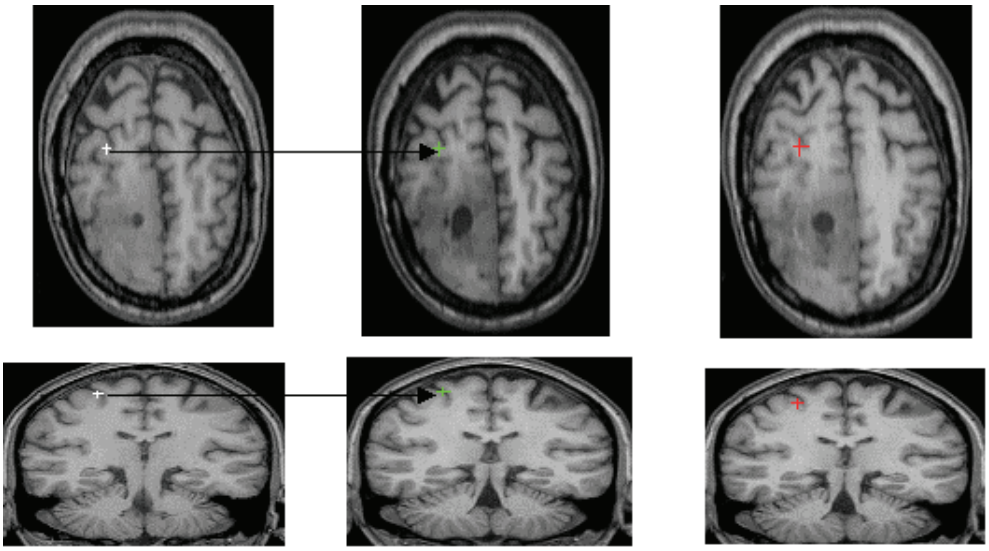

FIG. 4. LANDMARK REGISTRATION. *Two serial scans of a human subject with progressive low-grade glioma that are approximately* 2.5 *years apart. From left to right: the first column two landmarks manually placed by an expert in the early scan; the second column shows the two landmarks manually tracked by the same expert in the later scan. Finally, the third column shows the corresponding model-generated landmarks, for a given choice of the model parameters.*

The Eulerian description of the deformation field is denoted by $\boldsymbol{\psi}$. Using $\boldsymbol{\psi}$, we can track the target landmarks, or we can use it for an intensity-based registration function [8].

As mentioned, we optimize for a small number of parameters given the very sparse data. We solve for four parameters: the control of the initial tumor, the white matter tumor diffusivity and reactivity, and the force-coupling constant. Thus, $\boldsymbol{g} = (c_0, D_w, \rho, p_1)$. Also, white matter diffusivity changes the gray matter value, since we set the white matter diffusivity five times higher than that of the gray matter [50].

Notice that we are using an l_1-tracking functional. We do so because we compare our work to prior work in which the l_1 norm was used [26, 46]. We can solve this constrained-optimization problem by deriving the Euler–Lagrange optimality conditions of (2.6) and arrive at a set of PDEs for the forward, adjoint, and inversion parameters. (We also need to appropriately reformulate the nondifferentiable l_1-tracking.) We have used such an approach in a study for the 1D case [30], in which we solved a distributed parameter problem for the initial condition of the tumor using PDE-constrained optimization algorithms [9]. Since we optimize for four parameters only, we have opted for a derivative-free optimization method that requires only function evaluations. Every evaluation of the objective function requires a forward solve. We have used `APPSPACK`, a derivative-free optimization library from Sandia National Laboratories [22, 35, 36]. `APPSPACK` allows for bound constrains on the optimization variables and is suitable for our problem. In all of our experiments we used `APPSPACK` solver version 5.0.

The optimization variables should lie within a physiological range. Their precise range, however, is unknown. For example, the reaction term in our tumor model is a simple qualitative approximation of tumor growth that *does not have predictive capabilities*. Also, even if the model were correct, there would be significant

interindividual variability. We used values from existing literature for the tumor cell diffusivity in white and gray matter. We use numerical experiments to determine acceptable ranges for ρ and p_1.

3. Numerical scheme for the forward problem. The forward problem couples linear elasticity coupled to reaction-advection-diffusion equations. Besides the nonlinear coupling, the problem is also complicated by the brain's complex geometry and the inhomogeneous material properties. We selected a scheme that is relatively easy to implement and is reasonably fast. Its basic components are (1) an operator-splitting for (2.1); (2) a semi-implicit scheme for the coupling between (2.1) and (2.2); (3) an explicit scheme for (2.4); (4) a penalty method to approximate the boundary conditions for (2.1) and (2.2); and (5) a geometric multigrid scheme for the scalar and vector elliptic solvers. Next, we give details first on the overall time-stepping scheme and then on the elliptic solvers.

Time stepping. To decouple the nonlinearities and simplify the implementation we time-split the tumor equation (2.1) into advection, diffusion, and reaction steps [53, 54]. We have implemented one scalar and vector elliptic solver, two hyperbolic solvers (one for the conservative mass transport and another for the nonconservative advection of material properties), and the reaction step.

Let T be the total simulation time and Δt the time step. Given $c^n, \mathbf{u}^n, \mathbf{v}^n, \mathbf{m}^n$, the update $c^{n+1}, \mathbf{u}^{n+1}, \mathbf{v}^{n+1}, \mathbf{m}^{n+1}$ is computed as follows:

(1) $\mathbf{m}^{n+1} = \mathbf{m}^n - \Delta t(\nabla \mathbf{m}^n)\mathbf{v}^n$;

(2) $c^* = c^n - \Delta t \nabla\cdot(c^n \mathbf{v}^n)$;

(3) $c^{**} + \Delta t \nabla\cdot(D^{n+1}\nabla c^{**}) = c^*$;

(4) $c^{n+1} + \Delta t \rho c^{n+1}\,(1 - c^{n+1}) = c^{**}$;

(5) $\nabla \cdot ((\lambda^{n+1}\nabla \cdot \mathbf{u}^{n+1}) + \mu^{n+1}(\nabla \mathbf{u}^{n+1} + (\nabla \mathbf{u}^{n+1})^T)) = f(c^{n+1})c^{n+1}$;

(6) $\mathbf{v}^{n+1} = \dfrac{\mathbf{u}^{n+1} - \mathbf{u}^n}{\Delta t}$.

In the case of small diffusion, step (3) can be carried out explicitly. In step (1), the material properties are advected using a first-order upwind finite difference scheme (see [49, p. 29]; we use a staggered grid approach, since the material properties are constant at each voxel. In step (2) the divergence is discretized using a conservative finite-difference scheme; the diffusion and elasticity operators are discretized by finite elements. Our scheme has a CFL time-step restriction, due to the operator split, and explicit marching [47]. Overall we have 10 unknowns per grid point, if we include the deformation map $\boldsymbol{\psi}$, and the accuracy of the scheme is first order in time and second order in space.

Elliptic solvers and boundary conditions. Since we are interested in the large-deformations case, we have opted for a regular grid imposed on the image, and an Eulerian formulation that does not require remeshing. One complication, however, is that we need to impose Neumann conditions (diffusion) and Dirichlet conditions (elasticity) at the skull. Following [2, 21, 28], we use a penalty approach in which the target domain (brain) ω is embedded on a larger computational rectangular domain (box). We approximate diffusion Neumann conditions using a material with very low diffusivity in the exterior of the skull, and we approximate Dirichlet conditions by

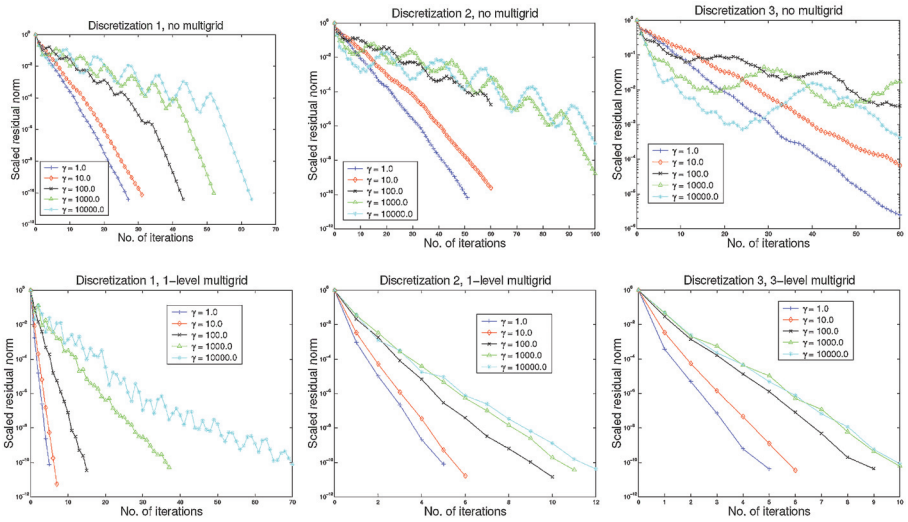

FIG. 5. MULTIGRID PERFORMANCE FOR LINEAR ELASTICITY. *To demonstrate the performance of the solver we reproduce this figure from* [27]. *We solved an elasticity problem with inhomogeneous material properties. The top row depicts the relative residual convergence history for the single-level incomplete LU preconditioned case for the mesh sizes of* 17 *(discretization* 1*),* 35 *(discretization* 2*), and* 65 *(discretization* 3*) nodes per dimension (from left to right); the bottom row depicts results for the multigrid case. We observe good algorithmic scalability for high contrasts; the number of multigrid iterations is mesh independent.*

using a very stiff material in the exterior of the skull as follows:

$$D_\epsilon = \left\{ \begin{array}{ll} D & \text{in } \omega \\ \epsilon D & \text{in } \Omega \backslash\, \overline{\omega} \end{array} \right\} \quad \text{and} \quad (\lambda, \mu)_\epsilon = \left\{ \begin{array}{ll} (\lambda, \mu) & \text{in } \omega \\ \frac{1}{\epsilon}(\lambda, \mu) & \text{in } \Omega \backslash\, \overline{\omega} \end{array} \right\}.$$

Here $\epsilon > 0$ is a "small" positive number, regarded as a penalty parameter. Then, the diffusion equation (2.1) on ω is replaced by its extension to Ω, with D replaced by D_ϵ and $\mathbf{v} = 0, \rho = 0$ in $\Omega \backslash\, \overline{\omega}$. A zero-flux boundary condition is imposed on $\partial\Omega$. The elasticity equation (2.2) on ω is replaced by its extension to Ω, with (λ, μ) replaced by $(\lambda, \mu)_\epsilon$ and $f \equiv 0$ in $\Omega \backslash\, \overline{\omega}$. A zero displacement boundary condition is imposed on $\partial\Omega$. The convergence to the solution of the original problem in the limit $\epsilon \to 0$ is shown in [57]. The expected order of convergence is at least $O(\sqrt{\epsilon})$ (in H^1) [17]. The resulting linear systems for the diffusion and elasticity are solved by flexible GMRES, preconditioned by a multigrid method. We use geometric multigrid with classical full-weighting and linear interpolation intergrid transfers. We smooth with a few conjugate gradient iterations preconditioned by a damped matrix-free block Jacobi. Representative results are depicted in Figure 5. We used four levels of a V-cycle for the elasticity solver. We used a single-level diagonal scaling preconditioner for the diffusion equation. The diffusion coefficient is quite small, so the elliptic solve is cheap. Our code is developed on top of `PETSc` [7], a scientific computing library from Argonne National Laboratory.[7]

As a simple verification of the algorithm, next we consider a synthetic test case. Consider the case of a 3D regular domain $[0, L_x] \times [0, L_y] \times [0, L_z]$, occupied by a material characterized by inhomogeneous diffusivity D and constant Lamé's coefficients.

[7] All restriction and prolongation operators as well as the smoothers were developed from scratch, as the default `PETSc` solvers assume assembled matrices.

TABLE 3.1
CONVERGENCE STUDY FOR THE PROPOSED NUMERICAL SCHEME. *The relative l_∞ error of the numerical solution with respect to the synthetic closed-form solution at the final time $T = 1$ shown. The results indicate first-order convergence.*

	$\|c_{an}\|_\infty^{rel}$	$\|u_{an}\|_\infty^{rel}$	$\|D_{an}\|_\infty^{rel}$
$h = 1/16, \Delta t = 1/2$	0.0263	0.2069	0.0630
$h = 1/32, \Delta t = 1/4$	0.0099	0.1080	0.0460
$h = 1/64, \Delta t = 1/8$	0.0048	0.0533	0.0271
$h = 1/128, \Delta t = 1/16$	0.0037	0.0271	0.0145

We assume the following expressions for the tumor concentration c_{an}, displacement field $\mathbf{u}_{an}$, velocity $\mathbf{v}_{an}$, and diffusion coefficient D_{an}:

$$c_{an}(x,y,z,t) = \frac{1}{4}c_0\left(1+\frac{t}{T}\right)(\cos(a_x x)+1) \quad \text{and} \quad \mathbf{u}_{an}(x,y,z,t) = (u_x,0,0);$$

$$u_x(x,y,z,t) = u_0\left(\frac{t}{T}\right)^2 \frac{x(L_x-x)\sin(a_x x)}{L_x^2}\frac{y(L_y-y)\sin(a_y y)}{L_y^2}\frac{z(L_z-z)\sin(a_z z)}{L_z^2};$$

$$\mathbf{v}_{an}(x,y,z,t) = \left(\frac{\partial u_x}{\partial t},0,0\right);$$

$$D_{an}(x,y,z,t) = D_0\frac{t}{T}\frac{y(L_y-y)}{L_y^2}\frac{z(L_z-z)}{L_z^2}$$

for $(x,y,z,t) \in [0,L_x]\times[0,L_y]\times[0,L_z]\times[0,T]$, with $a_x = \frac{\pi}{L_x}$, $a_y = \frac{\pi}{L_y}$, $a_z = \frac{\pi}{L_z}$ chosen such that c_{an} and $\mathbf{u}_{an}$ satisfy initial and boundary conditions. The results are summarized in Table 3.1; here we used the following parameter values: $L_x = L_y = L_z = 1, T = 1; c_0 = 1, u_0 = 0.1, D_0 = 0.01; \rho = 0.1, \lambda = 0.4, \mu = 0.2, p_1 = 0.1, p_2 = 0$. A uniform discretization was used in both space and time, with size h and Δt, respectively. First-order convergence rates are observed.

4. Application to 3D MR brain images. In this section, we report results from numerical experiments on synthetic and real datasets. In section 4.1, we demonstrate the ability of the method to produce complex deformation fields while varying only a few parameters. In section 4.1.1, we conduct numerical experiments in which we detect multiple minima that show that the optimization problem is nonconvex, independently of the number of landmarks. In section 4.2, we apply the method to real datasets, in which we measure errors by comparing the computed displacements to manually reconstructed landmark displacements, and we compare the method with simpler models previously developed in our group. Also, we conduct a simple cross-validation study.

For each experiment, we are given a longitudinal set of images with progressively higher tumor concentration. This set is segmented to white and gray matter, ventricles, and cerebrospinal fluid. Also, we assume that a set of landmarks is tracked in each image in the dataset, and thus displacements at certain positions are recovered. Finally, we assume that the tumor center is given in the *initial frame only*. In our real datasets, the tumors are almost spherical; detecting the tumor center is quite easy (1–2 voxels rater variability) by detecting the slice of maximum tumor diameter in the three coordinate planes.[8]

[8]This approach, however, is not general, as in practice most tumors have rather complicated shapes and the notion of a "tumor center" is not well defined.

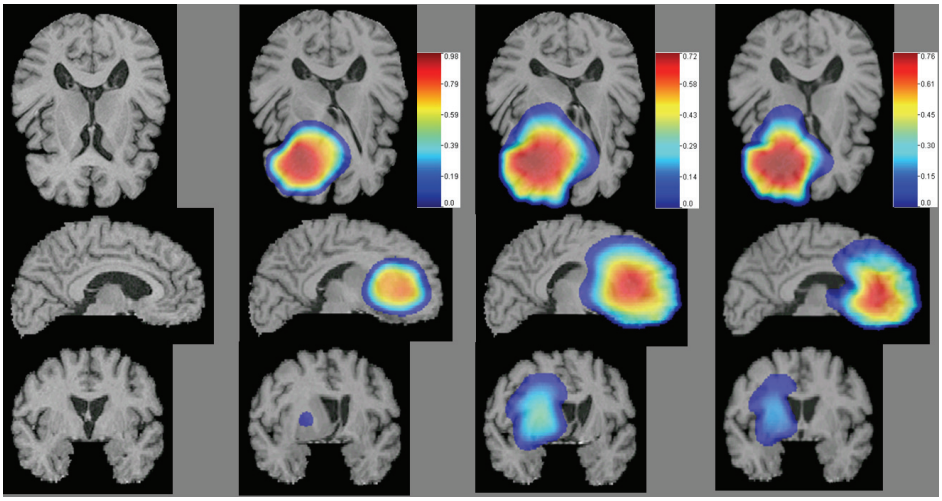

FIG. 6. SYNTHETIC SIMULATIONS OF GLIOMA GROWTH. *In this figure, we depict results from synthetic simulations of glioma growth located at the right frontal lobe. We report three different case scenarios starting from the same initial tumor seed. Left to right: The first column illustrates the 3D MRI of a normal brain image—axial, sagittal, and coronal section, respectively. The second column shows the deformed image, with simulated tumor corresponding to low tumor diffusivity and long-range mass effect ($p_2 = 0$). The third column shows the deformed image, with simulated tumor corresponding to high tumor diffusivity (10 times higher) and long-range mass effect ($p_2 = 0$). Finally, the fourth column shows the deformed image, with simulated tumor corresponding to high tumor diffusivity and short-range mass effect ($p_2 = 0.1$). The tumor maps are overlaid on the deformed template. In all three case scenarios, the run time is about 500 seconds on a 2.2GHz AMD Opteron.*

Given the segmented image labels, we assign piecewise constant material properties accordingly (white matter, gray matter, ventricles, cerebrospinal fluid) for each voxel. These values are used as the initial condition in the transport equations (2.4). The 3D computational domain in this case is the underlying domain of the image. In all of our experiments, we use $E_{white} = 2100\,\text{Pa}$ and $E_{ventricles} = 500\,\text{Pa}$ for the Young's modulus for the white matter and ventricles, respectively, and $\nu_{white} = 0.45$ and $\nu_{ventricles} = 0.1$ for the Poisson's ratio for the white matter and ventricles, respectively.

The goal of all our simulations is to reproduce the displacement field and not to reproduce the tumor dynamics. The tumor model we use is too simplistic and serves as a coarse qualitative approximation to the tumor growth.

4.1. Synthetic brain-tumor images. Consider a normal brain template, as shown in Figure 6 (leftmost column). The segmented brain here consists of white matter, gray matter, cerebrospinal fluid, and the ventricles (also filled with cerebrospinal fluid). The tumor diffusivity in the white matter was set five times higher than in the gray matter [50], while the diffusivity in the ventricles and cerebrospinal fluid was set to zero. (The elastic parameters are discussed in the beginning of this section.) These simulations correspond to an aggressive physical tumor growth over $T = 365$ *days*, starting from the same Gaussian initial tumor seed of center $\mathbf{x}_0 = (x, y, z) = (0.095, 0.07, 0.093)$ (m) in the right frontal lobe. The numerical solution was obtained using 10 time steps and 65^3 grid points. The tumor growth illustrated in the second column (left to right) of Figure 6 is less diffusive

($D_w = 7.5\times10^{-8}\ m^2/day$; $D_g = 1.5\times10^{-8}\ m^2/day$) and more regularly shaped, while in the other two case scenarios depicted in the third and fourth columns (left to right), respectively, we increased the diffusivity by a factor of 10 ($D_w = 7.5 \times 10^{-7}\ m^2/day$; $D_g = 1.5 \times 10^{-7}\ m^2/day$). This case corresponds to a scenario where strong mass effects are present, but far from the tumor core. These long-range effects can be well observed by examining the ventricle deformation in the corresponding axial slices. If p_2 is increased, the mass effects are more localized to areas close to the tumor core. This can be observed in the fourth column of Figure 6; we refer to such mass effects as "short-range." The rest of the model parameters are kept fixed to $\rho = 0.036\ day^{-1}$, $p_1 = 15kPa$, $p_2 = 2$. More complex tumor patterns could be obtained by using more complicated initial tumor profiles and anisotropic diffusion, which can be achieved by utilizing information from diffusion tensor MRI. In conjunction with the reduced computational cost, this translates into a versatile and robust simulation tool.

4.1.1. Analysis of the parameter estimation problem on synthetic brain data. Consider now a parameter estimation problem associated with the above synthetic brain tumor simulations in a normal brain template. We conduct a numerical study to illustrate the nonconvexity of the registration problem as a function of the number of landmarks and the effect of imposing bound constraints. The initial tumor volume is roughly 900 voxels. The total brain volume is approximately 953K voxels. The total simulation time is $T_l = 180\ days$. The original MR image (normal brain template) in this case is $256^2 \times 124$ voxels, with a physical voxel size of 0.9375^3mm$\times$1.5 mm. The tumor cell diffusivity in the gray matter is assumed to be five times slower than in that of the white matter and equal to zero in the ventricles and the cerebrospinal fluid.

We use 65^3 grid points and three time steps.[9] We generate a number of synthetic landmarks (20, 80, and 160) by running the forward problem with a set of fixed values of the optimization parameters. The results were generated setting $c_0 = 0.2$, $p_1 = 5$, $D_w = 1.0\times10^{-7}$, and $\rho = 0.1/day$—an "aggressive" tumor growth scenario—to simulate a pronounced mass effect. The bounds on the optimization parameters are selected based on physiological correctness (positive diffusion), on values reported in the literature, and by numerical experimentation for different images and tumor sizes. In Figure 7, we report the value of the landmark mismatch functional for different values of D_w (different curves) and ρ (points within each curve) and for different numbers of landmarks. The point of this figure is not so much the precise values, but rather the existence of multiple minima. Given this parametric study, we then use those values to test the optimizer by considering two scenarios. In the first scenario, the imposed bounds are relatively tight with respect to the diffusion and growth parameters D_w and ρ, respectively, corresponding to actual tumor physical parameters $D_w \in [1.0 \times 10^{-7}, 5.0 \times 10^{-7}]\ m^2/day$ and $\rho \in [0.05, 0.15]\ day^{-1}$. In the second scenario, these bounds were relaxed to $D_w \in [1.0 \times 10^{-8}, 5.0 \times 10^{-6}]\ m^2/day$ and $\rho \in [0.05, 0.5]\ day^{-1}$. All other `APPSPACK` solver options (e.g., initial guess, step tolerance) were kept fixed at their default values. The number of function evaluations (and thus, forward solves) was between 88 (20 landmarks) and 271 (160 landmarks).

The results show that in the tight-bounds case the original set of four model parameters was correctly retrieved by the optimizer—even when using only 20

[9] Increasing the number of time steps did not show any significant impact on the solution of the parameter-estimation problem.

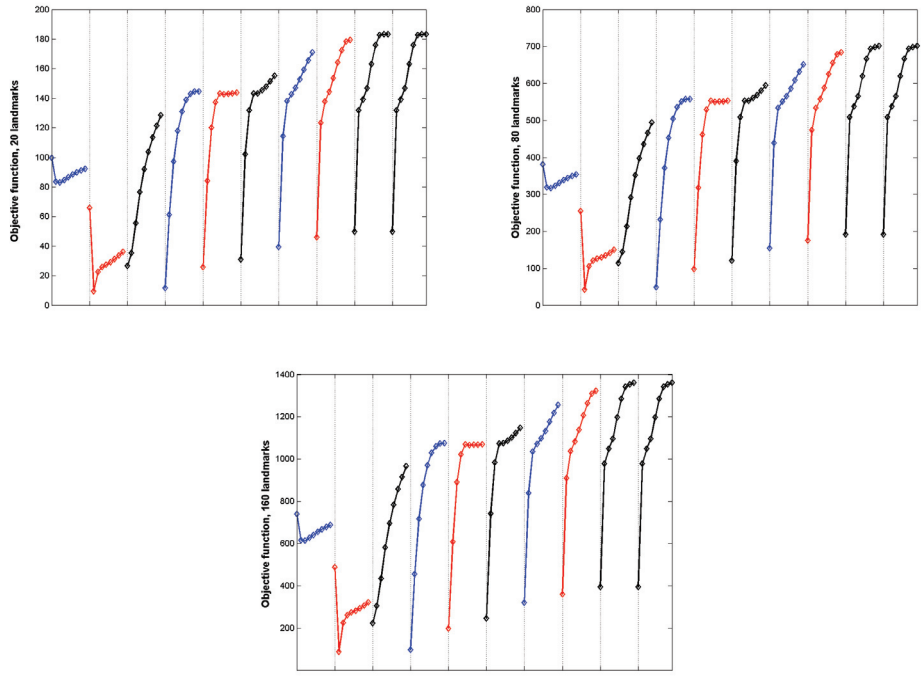

FIG. 7. NONCONVEXITY. *Here we conduct a parametric study of the objective function landscape for* 20, 80, *and* 160 *landmarks, respectively. In each curve, we vary* ρ *and* D_w *across different curves. We have observed two distinct minima that are insensitive to the number of landmarks. In the set of experiments in which the* $\boldsymbol{g}$ *bounds were relatively tight with respect to the diffusion and growth parameters* D_w *and* ρ *(*$D_w \in [1.0\times10^{-7}, 5.0\times10^{-7}]$ m^2/day *and* $\rho \in [0.05, 0.15]$ day^{-1}*), the correct solution was recovered by the optimizer—even with the minimum number of* 20 *target landmarks. In a second set of experiments, with* $D_w \in [1.0\times10^{-8}, 5.0\times10^{-6}]$ m^2/day *and* $\rho \in [0.05, 0.5]$ day^{-1}*, the optimizer converged to a solution with* c_0 *and* p_1 *close to their true values, but with* D_w *and* ρ *quite different.*

landmarks. However, when the bounds were relaxed, the optimizer consistently converged to a different solution, independently of the number of landmarks used. In this second local minimum, the diffusivity is about 10 times lower, while the growth rate is about two times higher. Thus, it appears that, based on landmark information only, we get different local minima corresponding to different physical tumor growth scenarios, such as high diffusivity/low growth rate versus lower diffusivity/higher growth rate. In such cases, additional information is needed to select the right physical solution. In conclusion, unless richer datasets become available, more complex tumor–brain models cannot be validated.

4.2. Landmark-based parameter estimation on real datasets. In [28] and [26], we tested a strictly mechanical model to reproduce mass effects caused by actual brain tumors in two dog cases with surgically transplanted glioma cells and in a human case with progressive low-grade glioma. Here, we use the same datasets for validation and comparison purposes. For the two dogs (DC1 and DC2), a baseline scan was acquired before tumor growth, followed by scans on the 6th and 10th days postimplantation. Gadolinium-enhanced T1 MR images were acquired. By the 10th day, tumors grew rapidly to a diameter of 1–2 cm, and then the animals were

TABLE 4.1

LANDMARK REGISTRATION ERRORS. *Landmark errors for the two dog cases (DC1, DC2) and for the human case (HC) with the new model (optimized). The errors reported here were computed with respect to the deformations of landmarks that were manually placed and tracked by an experienced human rater. Both the incremental pressure model and the new model were numerically solved using a spatial discretization with* 65^3 *nodes; five pressure increments were applied in the simple pressure model; four time steps were used in the new model for the two dog cases and five equal time steps were used for the human case.*

Landmark error (mm)	Median	Min	Max	Run time (sec)
New model DC1	0.89564	0.0511	1.9377	200
Incremental pressure model	1.6536	0.3176	2.6491	300
Inter-rater variability DC1	0.8484	0.1304	2.8568	
New model DC2	1.2980	0.3803	2.6577	200
Incremental pressure model	1.8912	0.4795	3.7458	300
Inter-rater variability DC2	1.3767	0.1226	2.7555	
New model HC	1.8457	0.5415	4.1451	250
Incremental pressure model	5.23	1.15	8.9	300

sacrificed (prior to any neurological complications). For the human case (HC), two T1 MRI scans taken 2.5 years apart were available (Figure 10). In all three cases, pairs of corresponding landmark points were manually identified by human raters in the starting and target images. The landmarks were nearly uniformly distributed outside the core of the tumor and within a distance of two tumor diameters. For the dog cases, two human raters placed independent sets of landmarks. All the results reported here are with respect to the most experienced rater of the two; the inter-rater variability is included in Table 4.1. For the human case, only one human rater was available.

The initial tumor location (its center and approximate size) can be estimated from the early scan. We report the aggregate landmark registration error in *mm* in Table 4.1. Relative landmark errors with respect to the maximum landmark displacement for both the simplified incremental pressure approach and the new model are shown for comparison in Figure 8. The corresponding average relative improvements achieved by the new (optimized) model are 17%, 20%, and 51% for DC1, DC2, and HC, respectively. A visual illustration of simulations via the two different approaches (new model versus incremental pressure) is shown in Figure 9, highlighting the potential of the new model to capture more information about the tumor compared to our previous approach.

4.2.1. Cross-validation results for the human case. In our previous test, we used all available landmark information to invert for the unknown parameters. We obtained results that indicate that our proposed multiphysics modeling framework can reasonably fit actual brain tumor subject data. A more stringent test for the model is to avoid using all the landmarks in the available dataset.

To investigate the predictive capabilities of the proposed model, we conducted a leave-one-out cross-validation experiment for the human case. A total of 21 pairs of manually placed landmarks were available. In the cross-validation test, we solve the parameter-estimation problem for values of $\boldsymbol{g}$ parameters (c_0, D_w, ρ, p_1) that minimize the objective functional based on 20 pairs of corresponding landmarks and compute the error for the remaining 21st target landmark that has not been included in the optimization.

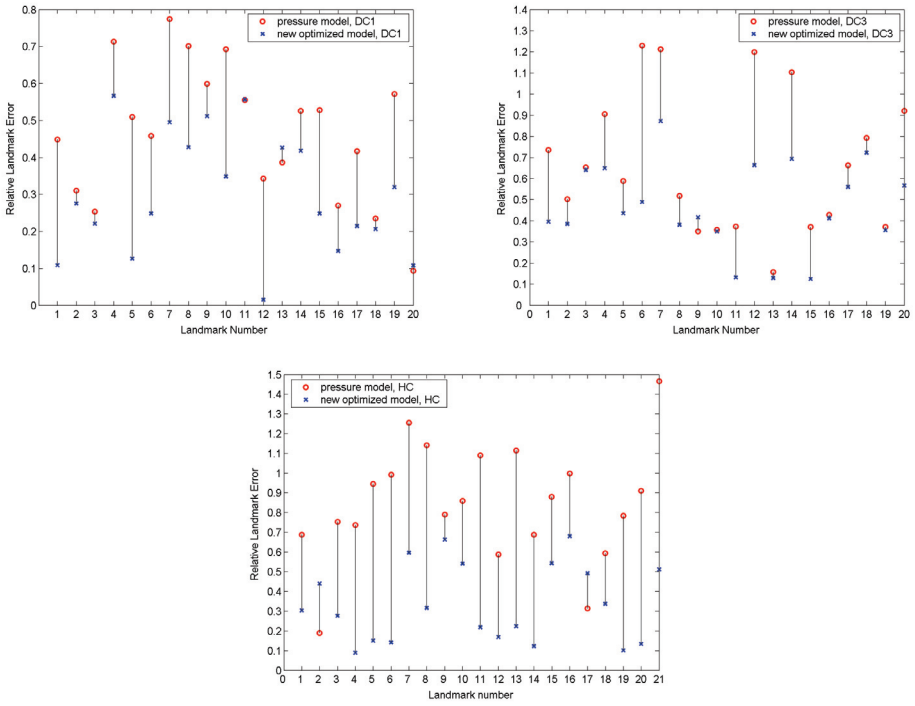

FIG. 8. RELATIVE ERROR FOR LANDMARK REGISTRATION. *Comparison of relative landmark errors (here with respect to the maximum landmark displacement) for the three cases DC*1*, DC*2*, and HC via the incremental pressure approach and the new model. The corresponding average relative improvements achieved by the new optimized model are* 17%*,* 20%*, and* 51% *for DC*1*, DC*2*, and HC, respectively.*

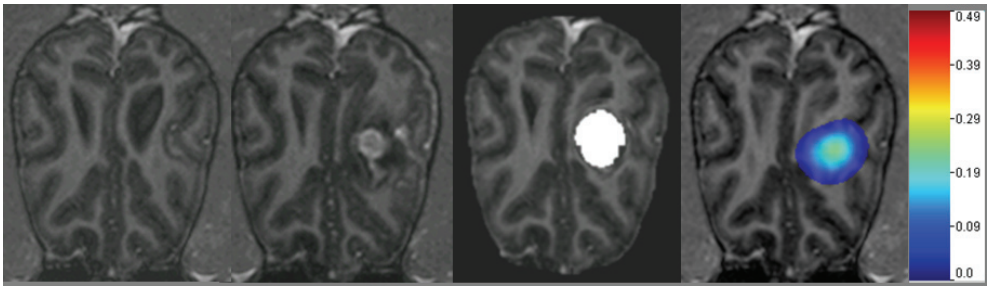

FIG. 9. REAL BRAIN TUMOR IMAGES FOR DOG CASE DC1. *From left to right: Starting scan, T*1 *MR gadolinium enhanced; target scan, T*1 *MR gadolinium enhanced; our simulated tumor growth and mass effect via the new optimized framework (tumor color maps overlaid on the model-deformed image, with corresponding bar attached); simulated mass effect via the simplified incremental pressure approach in* [28]*, with tumor mask highlighted in white. While the deformation pattern is, visually, only slightly different, the new tumor growth model shows potential for capturing more information about the tumor compared to the pressure approach. Note that the tumor mask should not be interpreted as a prediction of the tumor concentration. Rather, it represents the area of uncertainty in which deformations are not expected to be recovered in any degree of accuracy.*

The initial tumor volume is approximately 7800 voxels and the brain volume of $793K$ voxels; $T_l = 900$ *days*. The image resolution is $256^2 \times 124$ voxels, each voxel being $0.9375^2 \times 1.5$ mm. In a first set of leave-one-out experiments, we have used

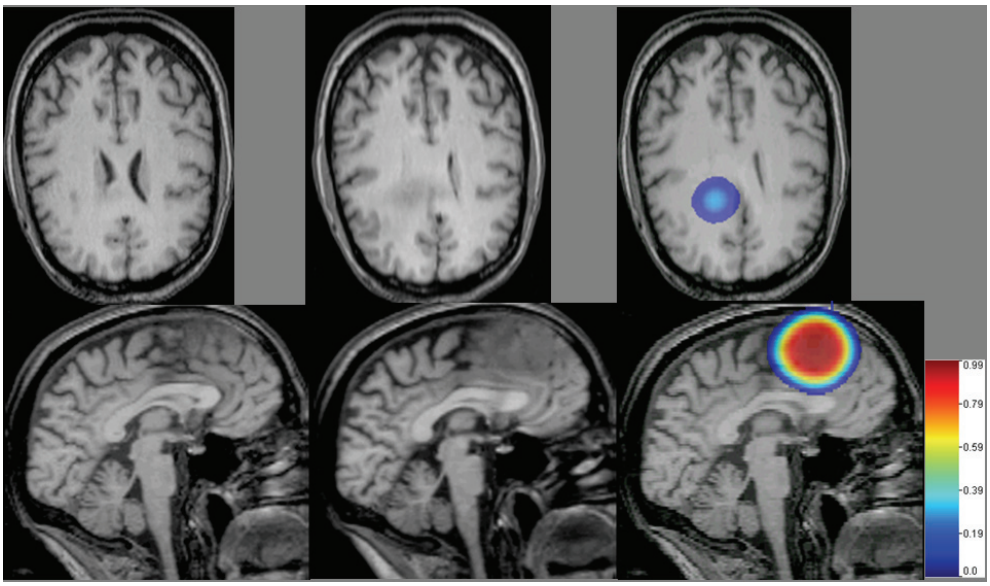

FIG. 10. REAL BRAIN TUMOR IMAGES, HUMAN SUBJECT *Left to right: starting scan, T1 MR; target scan, T1 MR; our simulated tumor growth and mass effect via the new optimized framework: tumor color maps overlaid on the model-deformed image, with corresponding color bar attached. Reasonable visual agreement obtained between the deformations in the actual patient target image (second column) and the simulated one (third column, right), guided by only 21 pairs of corresponding landmarks manually placed by a human rater in the early scan and the late (target) scan, respectively. Note that in this case, the brain was segmented into white matter and ventricles only, which explains the quasi-uniform tumor growth pattern.*

the same bounds on $\boldsymbol{g}$ as those shown in Figure 8. The results from this test are reported in Figure 11. They indicate reasonable model predictability for relatively tight bounds imposed on the four optimization variables. The corresponding average landmark error (physical, mm) upon cross validation here is 2.23 mm. The manually placed landmark displacement statistics in this case, included here for comparison, are $median = 4.15\ mm$, $min = 3.19\ mm$, and $max = 6.1\ mm$.

In a second set of cross-validation experiments, we relaxed the bounds on the four optimization variables; the solution is depicted in Figure 11. Along similar lines with the results obtained on the synthetic brain data in section 4.1.1, the results indicate that under extremely relaxed bounds, the problem has multiple local minima. Distinct trends of solutions are observed: one corresponding to a tumor growth scenario characterized by lower initial tumor density, higher diffusivity, lower growth rate, and with strong mass effect due to tumor infiltration; and another solution corresponding to tumor growth characterized by high initial tumor density, low diffusivity, high growth rate, and mass effect caused mainly by tumor bulk. Additional information about the tumor is needed in order to uniquely reconstruct a solution.

5. Conclusions and further research. We have proposed a constrained-optimization formulation for the coregistration of tumor-bearing brain images. We proposed a framework for modeling glioma growth and the subsequent mechanical impact on the surrounding brain tissue, the so-called mass effect.

The long-term goals of this work are (1) to improve the deformable registration from a brain tumor patient image to a common stereotactic space (atlas) with the

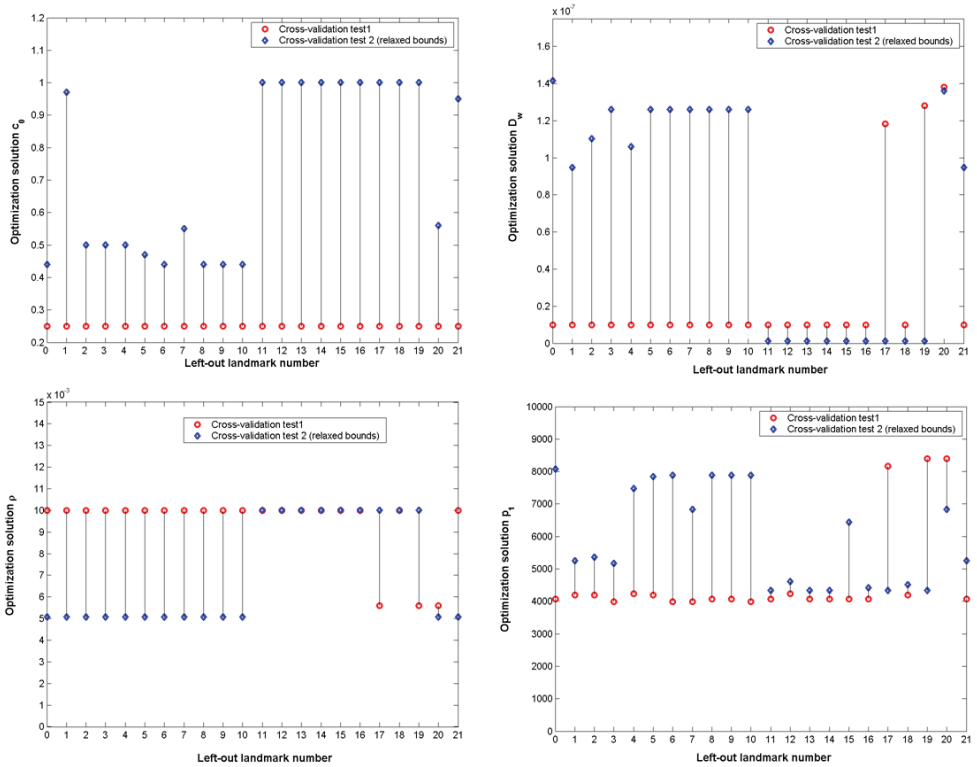

FIG. 11. CROSS VALIDATION. *We report results from the leave-one-out cross-validation experiment for two cases, a first case (test* 1*) with tight bounds on the inversion parameters, and a second case (test* 2*) with relaxed bounds on the inversion parameters. The results for the first case indicate reasonable model predictability when tight bounds were imposed on* $\boldsymbol{g}$*. The corresponding average landmark error (physical, mm) upon cross validation is* 2.23 *mm. These results for the second case indicate that without tight constraints we obtain multiple local minima, which correspond to different tumor growth physical scenarios.*

ultimate purpose of building statistical atlases of tumor-bearing brains; and (2) to investigate predictive features for glioma growth after the model parameters are estimated from given patient scans. The first is important for integrative statistical analysis of tumors in groups of patients and for surgical planning. The second is important for general treatment planning and prognosis.

We discussed numerical algorithms for solving the nonlinear systems of PDEs governing the proposed unified model. The numerical solution procedure is designed to be readily applied to 3D images of brain tumor subjects. These problems can result in very large deformations. To avoid remeshing, we have employed a structured grid discretization. We illustrated the capabilities and flexibility of the method in capturing complex tumor shapes and the subsequent mass effect with reasonable computational cost. We tested both the model and the automatic optimization framework on synthetic datasets and real brain tumor datasets and showed improvement compared to existing approaches with less realistic models. (Of course, our model is still a very rough approximation of true biophysics). In our numerical experiments, we observed nonconvexity; one way to address it is by imposing strict lower and upper bounds. We are currently integrating the code with more complex similarity functions and

multiple imaging modalities.

Overall the results are quite preliminary and inconclusive. The tumor model is by no means predictive and quantitatively accurate. Our goal in this article is to showcase an example in which several aspects of computational mathematics are used in a practical setting. In the context of image registration for tumor-bearing images, a significant amount of additional work is necessary before one can draw conclusions on the clinical applicability of our approach.

First, we need to conduct sensitivity analysis of the solution with respect to segmentation and elastic material properties of the brain and the tumor tissues. Second, we need to have more general parametrizations for the initial profile of the tumor. In fact, one should not invert for the initial conditions, but rather for a forcing term (with compact support, in time) that models the initial occurrence of tumor, which in general takes place in an unknown moment in time. The current optimization solver is robust, but slow; we require hundreds of function evaluations, and this will be a significant bottleneck as we introduce more optimization variables. For example, in our formulation we considered a single-degree-of-freedom parametrization of the initial tumor concentration; richer representations are necessary for batch processing of images. We are currently implementing fast PDE-constrained optimization algorithms.

From a practical point of view, serial scans of human subjects with gliomas progressing into higher malignancy are rare, although some clinical studies have been conducted [39]. Instead, animal experiments are necessary to construct more physiologically correct models. Such datasets can be employed in conjunction with our proposed framework for a preliminary validation/calibration of our image registration framework. Most important, rich longitudinal datasets will enable incorporation and validation of more sophisticated tumor models that include diffusive anisotropy, edema, necrosis, angiogenesis, and chemotaxis.

REFERENCES

[1] E. C. Alvord, Jr., and C. M. Shaw, *Neoplasms affecting the nervous system of the elderly*, in The Pathology of the Aging Human Nervous System, S. Duckett, ed., Lea and Febiger, Philadelphia, 1991.

[2] P. Angot, H. Lomenède, and I. Ramière, *A general fictitious domain method with non-conforming structured meshes*, in Proceedings of the International Symposium on Finite Volumes IV, Hermes Science, Cachan, France, 2005, pp. 261–272.

[3] R. Araujo and D. McElwain, *A history of the study of tumor growth: The contribution of mathematical modeling*, Bull. Math. Biol., 66 (2004), pp. 1039–1091.

[4] R. P. Araujo and D. L. S. McElwain, *A mixture theory for the genesis of residual stresses in growing tissues* I: *A general formulation*, J. Appl. Math., 65 (2005), pp. 1261–1284.

[5] J. Ashburner, J. Csernansky, C. Davatzikos, N. Fox, G. Frisoni, and P. Thompson, *Computer-assisted imaging to assess brain structure in healthy and diseased brains*, The Lancet (Neurology), 2 (2003), pp. 79–88.

[6] R. Bajcsy, R. Lieberson, and M. Reivich, *A computerized system for the elastic matching of deformed radiographic images to idealized atlas images*, J. Comput. Assisted Tomography, 7 (1983), pp. 618–625.

[7] S. Balay, K. Buschelman, L. Dalcin, V. Eijkhout, W. D. Gropp, D. Karpeev, D. Kaushik, M. Knepley, L. C. McInnes, B. F. Smith, and H. Zhang, *PETSc home page*, http://www.mcs.anl.gov/petsc (2007).

[8] M. F. Beg, M. Miller, A. Trouve, and L. Younes, *The Euler-Lagrange equation for interpolating sequence of landmark datasets*, in Medical Image Computing and Computer-Assisted Intervention (Miccai 2003), Pt. 2, Lecture Notes in Comput. Sci. 2879, Springer-Verlag, Berlin, 2003, pp. 918–925.

[9] G. Biros and O. Ghattas, *Parallel Lagrange–Newton–Krylov–Schur methods for PDE-constrained optimization. Part* I: *The Krylov-Schur solver*, SIAM J. Sci. Comput., 27 (2005), pp. 687–713.

[10] H. M. Byrne, J. R. King, D. L. S. McElwain, and L. Preziosi, *A two-phase model of solid tumor growth*, Appl. Math. Lett., 16 (2002), pp. 567–573.
[11] G. E. Christensen, S. Joshi, and M. Miller, *Volumetric transformation of brain anatomy*, IEEE Trans. Med. Imaging, 16 (1997), pp. 864–877.
[12] O. Clatz, M. Sermesant, P.-Y. Bondiau, H. Delingette, S. K. Warfield, G. Malandain, and N. Ayache, *Realistic simulation of the 3D growth of brain tumors in MR images coupling diffusion with mass effect*, IEEE Trans. Med. Imaging, 24 (2005), pp. 1334–1346.
[13] D. L. Collins, P. Neelin, T. M. Peters, and A. C. Evans, *Automatic 3D intersubject registration of MR volumetric data in standardized Talairach space*, J. Comput. Assisted Tomography, 18 (1994), pp. 192–205.
[14] V. Cristini and J. Lowengrub, *Nonlinear simulation of tumor growth*, J. Math. Biol., 46 (2003), pp. 191–224.
[15] M. B. Cuadra, C. Pollo, A. Bardera, O. Cuisenaire, J.-G. Villemure, and J.-P. Thiran, *Atlas-based segmentation of pathological MR brain images using a model of lesion growth*, IEEE Trans. Med. Imaging, 23 (2004), pp. 1301–1314.
[16] C. Davatzikos, D. Shen, A. Mohamed, and S. K. Kyriacou, *A framework for predictive modeling of anatomical deformations*, IEEE Trans. Med. Imaging, 20 (2001), pp. 836–843.
[17] S. Del Pino and O. Pironneau, *A fictitious domain based general PDE solver*, in Numerical Methods for Scientific Computing, Proceedings of the Conference METSO-ECCOMAS, E. Heikkola, ed., CIMNE, Barcelona, 2003.
[18] J. C. Gee, D. R. Haynor, L. LeBriquer, and R. K. Bajcsy, *Advances in elastic matching theory and its implementation*, in Proceedings of the First Joint Conference on Computer Vision, Virtual Reality and Robotics in Medicine and Medial Robotics and Computer-Assisted Surgery (CVRMED-MRCAS '97), Lecture Notes in Comput. Sci. 1205, 1997, pp. 63–72.
[19] A. Gefen and S. S. Margulies, *Are in vivo and in situ brain tissues mechanically similar?*, J. Biomechanics, 37 (2004), pp. 1339–1352.
[20] A. Giese and M. Westphal, *Glioma invasion in the central nervous system*, Neurosurgery, 39 (1996), pp. 235–250.
[21] R. Glowinski, T. W. Pan, R. O. Wells, and X. D. Zhou, *Wavelet and finite element solutions for the Neumann problem using fictitious domains*, J. Comput. Phys., 126 (1996), pp. 40–51.
[22] G. A. Gray and T. G. Kolda, *Algorithm* 856: *APPSPACK* 4.0: *Asynchronous parallel pattern search for derivative-free optimization*, ACM Trans. Math. Software, 32 (2006), PP. 485–507.
[23] M. Gurtin, *An Introduction to Continuum Mechanics*, Academic Press, New York, 1981.
[24] S. Habib, C. Molina-Paris, and T. Deisboeck, *Complex dynamics of tumors: Modeling an emerging brain tumor system with coupled reaction-diffusion equations*, Phys. A Statist. Mech. Appl., 327 (2003), pp. 501–524.
[25] A. Hagemann, K. Rohr, H. Stiehl, U. Spetzger, and J. Gilsbach, *Biomechanical modeling of the human head for physically based, nonrigid image registration*, IEEE Trans. Med. Imaging, 18 (1999), pp. 875–884.
[26] C. Hogea, G. Biros, and C. Davatzikos, *Fast Solvers for Soft Tissue Simulation with Application to Construction of Brain Tumor Atlases*, Tech. report ms-cis-07-04, www.seas.upenn.edu/∼biros/papers/brain06.pdf (2006).
[27] C. Hogea, F. Abraham, G. Biros, and C. Davatzikos, *Fast solvers for soft tissue simulation with application to construction of brain tumor atlases*, submitted.
[28] C. Hogea, F. Abraham, G. Biros, and C. Davatzikos, *A framework for soft tissue simulations with applications to modeling brain tumor mass-effect in 3d images*, in Proceedings of the Medical Image Computing and Computer-Assisted Intervention Workshop on Biomechanics, Copenhagen, 2006.
[29] C. Hogea, G. Biros, F. Abraham, and C. Davatzikos, *A robust framework for soft tissue simulations with application to modeling brain tumor mass effect in 3D MR images*, Phys. Med. Biol., 52 (2007), pp. 6893–6908.
[30] C. Hogea, G. Biros, and C. Davatzikos, *An image-driven parameter estimation problem for a reaction-diffusion glioma growth model with mass effects*, submitted.
[31] C. Hogea, G. Biros, and C. Davatzikos, *A coupled diffusion-elasticity PDE-constrained framework for simulating gliomas growth: A medical imaging perspective*, presented at the SIAM Conference on Computational Science and Engineering (Costa Mesa, CA), 2007.
[32] C. Hogea, C. Davatzikos, and G. Biros, *An image-driven parameter estimation problem for a reaction-diffusion glioma growth model with mass effects*, J. Math. Biol., 56 (2008), pp. 793–825.

[33] Z. Hu, D. Metaxas, and L. Axel, *In vivo strain and stress estimation of the heart left and right ventricles from mri images*, Med. Image Anal., 7 (2003), pp. 435–444.
[34] A. R. Kansal, S. Torquato, G. Harsh IV, E. Chiocca, and T. Deisboeck, *Simulated brain tumor growth dynamics using a three-dimensional cellular automaton*, J. Theoret. Biol., 203 (2000), pp. 367–382.
[35] T. G. Kolda et al., *APPSPACK home page*, http://software.sandia.gov/appspack/version5.0.1 (2007).
[36] T. G. Kolda, *Revisiting asynchronous parallel pattern search for nonlinear optimization*, SIAM J. Optim., 16 (2005), pp. 563–586.
[37] S. Kyriacou, C. Davatzikos, S. Zinreich, and R. Bryan, *Nonlinear elastic registration of brain images with tumor pathology using a biomechanical model*, IEEE Trans. Med. Imaging, 18 (1999), pp. 580–592.
[38] K. E. Lunn, K. D. Paulsen, D. R. Lynch, D. W. Roberts, F. E. Kennedy, and A. Hartov, *Assimilating intraoperative data with brain shift modeling using the adjoint equations*, Med. Image Anal., 9 (2005), pp. 281–293.
[39] E. Mandonnet, J. Delattre, M. Tanguy, K. Swanson, A. Carpentier, H. Duffau, P. Cornu, R. Van Effenterre, E. Alvord, Jr., and L. Capelle, *Continuous growth of mean tumor diameter in a subset of grade* II *gliomas*, Annals of Neurology, 53 (2003), pp. 524–528.
[40] M. I. Miga, K. D. Paulsen, J. M. Lemery, S. D. Eisner, A. Hartov, F. E. Kennedy, and D. W. Roberts, *Model-updated image guidance: Initial clinical experiences with gravity-induced brain deformation*, IEEE Trans. Med. Imaging, 18 (1999), pp. 866–874.
[41] K. Miller and K. Chinzei, *Mechanical properties of brain tissue in tension*, J. Biomech., 35 (2002), pp. 483–490.
[42] K. Miller, K. Chinzei, G. Orssengo, and P. Bednarz, *Mechanical properties of brain tissue in-vivo: Experiment and computer simulation*, J. Biomech., 33 (2000), pp. 1369–1376.
[43] M. I. Miller, A. Trouve, and L. Younes, *On the metrics and Euler-Lagrange equations of computational anatomy*, Ann. Rev. Biomed. Engrg., 4 (2002), pp. 375–405.
[44] J. Modersitzki, *Numerical Methods for Image Registration*, Oxford University Press, Oxford, UK, 2001.
[45] A. Mohamed, *Combining Statistical and Biomechanical Models for Estimation of Anatomical Deformations*, Ph.D. thesis, Johns Hopkins University, Baltimore, MD, 2006.
[46] A. Mohamed and C. Davatzikos, *Finite element modeling of brain tumor mass-effect from* 3*d medical images*, in Proceedings of Medical Image Computing and Computer-Assisted Intervention, Palm Springs, 2005 pp. 400–408.
[47] S. Osher and R. Fedkiw, *Level Set Methods and Dynamic Implicit Surfaces*, Springer, New York, 2003.
[48] X. Papademetris, A. J. Sinusas, D. P. Dione, R. T. Constable, and J. S. Duncan, *Estimation of* 3*-D left ventricular deformation from medical images using biomechanical models*, IEEE Trans. Med. Imaging, 21 (2002), pp. 786–800.
[49] P. Roache, *Computational Fluid Dynamics*, Hermosa, Albuquerque, NM, 1972.
[50] K. R. Swanson, E. C. Alvord, and J. D. Murray, *A quantitative model for differential motility of gliomas in grey and white matter*, Cell Proliferation, 33 (2000), pp. 317–329.
[51] K. R. Swanson, C. Bridge, J. D. Murray, and E. C. Alvord, *Virtual and real brain tumors: Using mathematical modeling to quantify glioma growth and invasion*, J. Neurolog. Sci., 216 (2003), pp. 1–10.
[52] P. Tracqui and M. Mendjeli, *Modelling three-dimensional growth of brain tumors from time series of scans*, Math. Models Methods Appl. Sci., 9 (1999), pp. 581–598.
[53] R. Tyson, L. Stern, and R. LeVeque, *Fractional step methods applied to a chemotaxis model*, J. Math. Biol., 41 (2000), pp. 455–475.
[54] J. Verwer, W. Hundsdorfer, and J. Blom, *Numerical Time Integration for Air Pollution Models*, Tech. report MAS-R9825, CWI, Amsterdam, 1991. Available online at http://ftp.cwi.nl/CWIreports/MAS/MAS-R9825.pdf.
[55] S. K. Warfield, F. Talos, A. Tei, A. Bharatha, A. Nabavi, M. Ferrant, P. Black, F. Jokesz, and R. Kikinis, *Real-time registration of volumetic brain MRI by biomechanical simulation of deformation during image guided neurosurgery*, Comput. Visual. Sci., 5 (2002), pp. 3–11.
[56] R. M. Wasserman, R. S. Acharya, C. Sibata, and K. H. Shin, *Patient-specific tumor prognosis prediction via multimodality imaging*, Proc. SPIE Int. Soc. Opt. Eng., 2709 (1996), pp. 468–479.
[57] S. Zhu, G. Yuan, and W. Sun, *Convergence and stability of explicit/implicit schemes for parabolic equations with discontinuous coefficients*, Internat. J. Numer. Anal. Model., 1 (2004), pp. 131–145.